

Article

Impact of the One-Stream Cloud Detection Method on the Assimilation of AMSU-A Data in GRAPES

Zhengkun Qin ¹ , Zhiwen Wu ¹ and Juan Li ^{2,3,*}

¹ Centre of Data Assimilation for Research and Application, Nanjing University of Information Science and Technology, Nanjing 210044, China; qzk_0@nuist.edu.cn (Z.Q.); 20191201084@nuist.edu.cn (Z.W.)

² National Meteorological Centre, China Meteorological Administration, Beijing 100081, China

³ Numerical Weather Prediction Centre, China Meteorological Administration, Beijing 100081, China

* Correspondence: lj@cma.gov.cn

Received: 18 October 2020; Accepted: 21 November 2020; Published: 23 November 2020



Abstract: Clouds affect the assimilation of microwave data from satellites and therefore the detection of clouds is important under both clear sky and cloudy conditions. We introduce a new cloud detection method based on the assimilation of data from the advanced microwave sounder unit A (AMSU-A) and the microwave humidity sounder (MHS) into the global and regional assimilation and prediction system (GRAPES) and use forecast experiments to evaluate its impact. The new cloud detection method can retain more observational data than the current method in GRAPES, thereby improving the assimilation of AMSU-A data. Verification of the method showed that, by improving the forecast of the lower-level air temperature and geopotential height, the new cloud detection method improved the forecast of the track of two typhoons. The forecast of a large-scale weather system in GRAPES was also improved by the new method in the later period of the forecast.

Keywords: AMSU-A; MHS; GRAPES; cloud detection

1. Introduction

The application of satellite data in numerical weather forecasting entered a new era when it became possible to directly assimilate satellite radiance data into a variational data assimilation system [1,2]. The direct assimilation of satellite data reduces the restriction caused by insufficient observational data. The continued increase in the amount of observational data from satellites and the improvement in assimilation methods has helped to improve the accuracy of the initial condition in numerical prediction models.

Microwave sounding data from satellites was first available from the microwave sounder unit (MSU) [3], followed by data from the advanced microwave sounder unit (AMSU-A/B), the microwave humidity sounder (AMSU-A/MHS) [4] and the advanced technology microwave sounder (ATMS) [5]. The AMSU-A and MHS are currently onboard the NOAA-18, NOAA-19 and European Meteorological Satellites Meteorological Operations Platform A, B, and C (MetOp-A, MetOp-B, and MetOp-C). The ATMS is currently onboard on the US Suomi-NPP and JPSS-1 satellites. Early Chinese FengYun meteorological satellites (e.g., FY-3A and FY-3B) carry the microwave temperature sounder-1 (MWTS-1), which is similar to the MSU, and the microwave humidity sounder-1 (MWHS-1). Since the launch of the FY-3C satellite on 23 September 2013, Chinese polar-orbiting meteorological satellites have been equipped with the MWTS-2 and MWHS-2, which have a unique practicability and higher horizontal resolution [6].

The AMSU-A data are currently the most influential observational data in almost all operational forecast systems. The assimilation of microwave sounding data can effectively improve global forecasts, especially in the southern hemisphere and oceanic areas [7–12]. The assimilation of AMSU-A data is

also widely used in regional weather forecasts, especially forecasts of extreme weather events, such as typhoons and heavy rainfall [13–17].

Because satellites observe the Earth from space, the application of satellite observations has always been restricted by clouds. Although microwaves can penetrate some clouds, measurements are affected by scattering and the reflection of the surface radiance by the clouds. However, because satellite data from cloudy areas contain abundant information about changes in the weather, it is important to assimilate radiance data from these regions and to describe the characteristics of clouds and their effects on microwave radiance data as reasonably as possible [18–23]. Many studies still focus on improving the assimilation of clear sky data due to the complexity of the influence of clouds and our insufficient understanding of the thermal and dynamic processes within them, as well as deficiencies in the ability of numerical models to simulate clouds [24–27].

An accurate method to detect clouds is a prerequisite for the effective assimilation of satellite data under both clear and cloudy skies and several effective cloud detection methods have been developed for the AMSU-A. For example, Bennartz et al. [28] used the brightness temperature of several AMSU-A and MHS channels to construct a scattering index to detect data contaminated by clouds. Cloud detection is applied in the gridpoint statistical interpolation assimilation system (GSI) based on a cloud liquid water path (LWP) index calculated from the brightness temperature difference between observation and simulation of channel 1 and 2 over ocean and channel 4 and 6 over land [29]. A scattering index is also used for detecting clouds in AMSU-A data in the global and regional assimilation and prediction system (GRAPES). However, these two cloud detection methods are empirical methods and lack a solid physical foundation, relying heavily on the background field. When the accuracy of the background field is poor, this leads to a significant bias in the simulated brightness temperature and the detection of clouds is prone to serious errors.

Zou et al. [30] merged the liquid water path (LWP) and the ice water path (IWP) physically retrieved from the AMSU-A and MHS measurement channels and proposed a one-stream cloud detection method over the ocean. The results were implemented in the gridpoint statistical interpolation assimilation system and the forecast results show that this new cloud detection method improved the forecast of rainfall in the advanced research weather research and forecasting model. However, this study only evaluated the impact of the one-stream cloud detection method on the assimilation of MHS data and only operated on the regional model covering the USA, so the global applicability of this method needs further research. Based on the latest version of the GRAPES global model, we introduced the AMSU-A and MHS one-stream cloud detection method into the GRAPES assimilation system and evaluated the impact of the new cloud detection method on the assimilation of AMSU-A data with the aim of improving the forecasting ability of GRAPES.

The structure of this paper is as follows. Section 2 introduces the GRAPES_GFS, 4DVAR assimilation system and the one-stream cloud detection scheme. Section 3 evaluates the effects of the one-stream cloud detection scheme. Section 4 describes the experimental design and the analysis of the results. Section 5 provides a summary and discussion.

2. Model and Methods

2.1. GRAPES System

China initiated the development of the new generation global/regional multiscale unified assimilation and prediction system GRAPES in 2001 and completed the development of the basic data assimilation and model prediction system over the next few years [31–34]. A global/regional unified three-dimensional variation (3DVAR) assimilation system was later established for GRAPES [35,36], followed by a 3DVAR assimilation system with coordinates and variable definitions that exactly match the GRAPES forecast model [37]. An operational 4DVAR assimilation system replaced the 3DVAR assimilation system in 2017. This system has been upgraded many times [37–39] and its

medium-term forecast performance is now better than that of the 3DVAR assimilation, especially in the southern hemisphere.

This work used GRAPES_GFS version 2.4. The prediction model uses a fully compressible, non-static equilibrium dynamic equation set in which the horizontal direction is the global latitude and longitude grid distributed for the Arakawa-C staggered network and the vertical direction uses terrain-following coordinates and the Charney–Phillips non-uniform layered discretization scheme with the two time-step semi-implicit and semi-Lagrangian algorithm. The GRAPES_GFS 2.4 data assimilation scheme is a 4DVAR scheme and uses an incremental analysis method. There are 60 vertical layers, the horizontal resolution is $0.25^\circ \times 0.25^\circ$ and the assimilation time-step is six hours. The GRAPES-4DVAR scheme selects the standardized pressure π or potential temperature θ , the zonal wind component u , the meridional wind component v and the specific humidity q as the analysis variables. The transformed flow function ψ , the unbalanced velocity potential function χ , the unbalanced dimensionless air pressure π_u , and the specific humidity q are used as the control variables.

2.2. One-Stream Cloud Detection Method over the Oceans

The AMSU-A has 15 channels and can detect the air temperature from the ground to the lower stratosphere, whereas the MHS has five channels and is mainly used to detect water vapor information in the mid- and lower troposphere. Table 1 shows the relevant information for each channel of the AMSU-A and MHS. The two low-frequency channels (channels 1 and 2) of the AMSU-A can be used to retrieve the LWP over the ocean, whereas the two high-frequency channels (channels 1 and 2) of the MHS can be used to retrieve the IWP over both the ocean and land [40,41]. If the AMSU-A and MHS data are combined into one stream of data, then information about the LWP and IWP can be obtained at the same time. Data contaminated by either water clouds or ice clouds can then be eliminated simultaneously.

Table 1. AMSU-A and MHS channel information.

Instrument	Channel	Central Frequency (GHz)	Polarization	Height of Peak Energy Contribution (hPa)
AMSU-A	1	23.80	V	Surface
	2	31.40	V	Surface
	3	50.30	V	Surface
	4	52.80	V	Surface
	5	53.59 ± 0.115	H	700
	6	54.40	H	400
	7	54.94	V	270
	8	55.50	H	180
	9	$f_0 = 57.29$	H	90
	10	$f_0 \pm 0.217$	H	50
	11	$f_0 \pm 0.322 \pm 0.048$	H	25
	12	$f_0 \pm 0.322 \pm 0.022$	H	12
	13	$f_0 \pm 0.322 \pm 0.010$	H	5
	14	$f_0 \pm 0.322 \pm 0.004$	H	2
	15	89.00	H	Surface
MHS	1	89.0	V	Surface
	2	157.0	V	Surface
	3	183.31 ± 1.0	V	800
	4	183.31 ± 3.0	H	600
	5	183.31 ± 7.0	H	400

The first step in the new cloud detection method is collocation. The AMSU-A and MHS are both cross-track microwave radiometers and the two instruments are usually carried on the same polar-orbiting satellite, so the time deviation between the two observations is negligible. The spatial

resolution of the AMSU-A at nadir is about 48 km, whereas the spatial resolution of the MHS is about 17 km. This means that one AMSU-A scan line can cover three MHS scan lines. This proportional relationship not only exists in the coverage of scan lines, but also in the spatial resolution of the field of view (FOV). The orbital width of the AMSU-A and MHS are about 2226.8 and 2348 km, respectively, and therefore there are 30 and 90 FOVs in each AMSU-A and MHS scan line, respectively. Although the spatial resolution of the FOV increases with the increase in the scan angle, the similar orbital widths retain the ratio of one to three between the spatial resolution of AMSU-A FOV and the MHS FOV. Collocation can therefore be easily achieved if it is assumed that one AMSU-A FOV corresponds to nine MHS FOVs.

Figure 1 shows the correspondence between the AMSU-A FOV (black circles) and the MHS FOV (red dots) of the NOAA-19 satellite in southeast Asia at 0000 h UTC on 9 August 2019. After the collocation, nine observations from the MHS are matched to one AMSU-A observation. The LWP and IWP can be retrieved from the collocated AMSU-A and MHS data simultaneously. The 2-m air temperature and surface winds from the background field are used as auxiliary data. For each AMSU-A FOV, the accumulated IWP retrieved from the nine collocated MHS FOVs is used as the IWP information. When either the LWP or IWP is >0.02 g/kg, the corresponding AMSU-A observation will be rejected as cloud-contaminated data. To evaluate the impact of the cloud detection method, only the AMSU-A data over clear skies are assimilated, so observations contaminated by clouds will be removed.

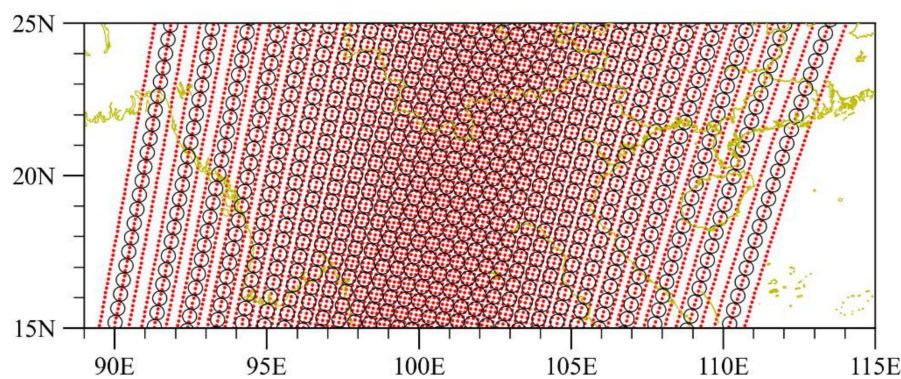


Figure 1. Spatial distribution of the observational position of the AMSU-A (black circles) and MHS (red dots) onboard the NOAA-19 satellite over southeast Asia at 0000 UTC 9 August 2019.

3. Evaluation of the One-Stream Cloud Detection Method

Figure 2 shows the spatial distribution of the LWP (Figure 2a) and IWP (Figure 2b) retrieved from the AMSU-A and MHS observations obtained by the MetOp-A satellite over southeast Asia during the time period 0900–1500 UTC 8 August 2019. Figure 2c shows the spatial distribution of the MODIS cloud classification products over southeast Asia between 0300 and 0900 UTC 8 August 2019. The MODIS cloud classification product was obtained by combining the cloud optical thickness and the cloud-top pressure in the MOD06_L2 product [42,43] Q. The most notable feature in Figure 2c is the large areas of cloud caused by two simultaneous typhoons, Lekima and Rosa, over the ocean to the east of China. Although there is a time lag between the two sets of data, it is clear from Figure 2 that the LWP accurately identifies the cloudy areas over the ocean, with the large value area of the LWP in the western Pacific Ocean corresponding to the deep convective spiral cloud masses of the typhoon and the convective cloud masses on the western side of the Philippines. The banded large LWP region in the northern Indian Ocean corresponds to deep convective and cirrocumulus clouds over the ocean. The extensive area covered by the large LWP in the southern Indian Ocean corresponds to cumulus and cirrus clouds over the ocean. The IWP is good at identifying deep convective and cirrus clouds over the ocean, especially the cirrus clouds missed by the LWP, such as those around the typhoons

and banded convective cloud systems in the upper right corner of the region. More accurate cloud detection results can therefore be obtained by combining the two streams of data.

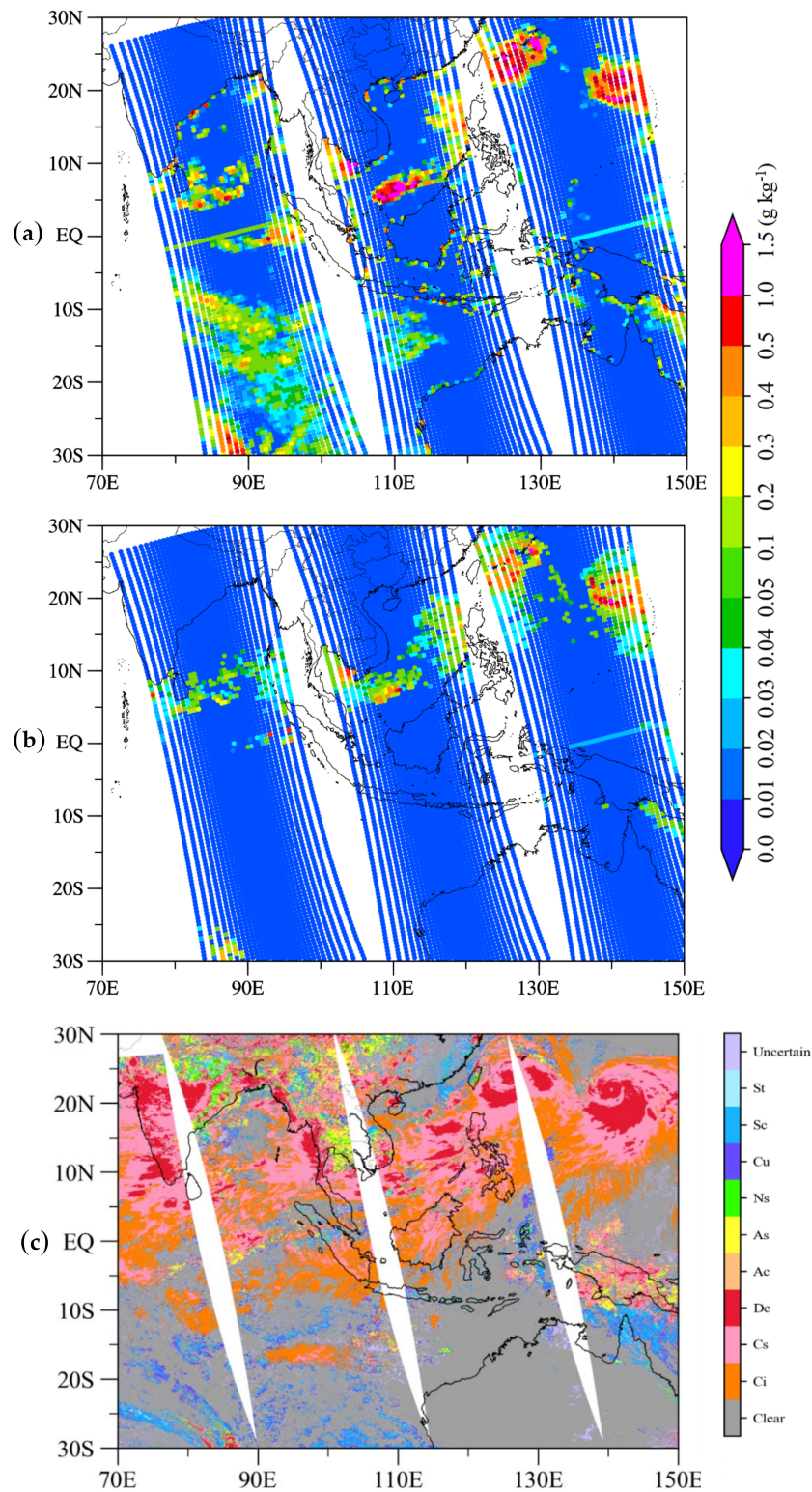


Figure 2. Spatial distribution of the integral whole-layer (a) LWP and (b) IWP from 0900 to 1500 UTC and (c) the MODIS cloud classification products during 0300–0900 UTC over southeast Asia on 8 August 2019.

To further verify the one-stream cloud detection method, the results were also compared with those obtained using the current cloud detection method in the GRAPES system. In this method, two criteria are used to remove cloudy AMSU-A data over the ocean. The first is the scattering index IS, which is defined as:

$$I_S = T_{EB15} - T_{B15}, \quad (1)$$

$$T_{EB15} = a + b \times T_{B1} + c \times T_{B2} + d \times T_{B3}. \quad (2)$$

where T_{B1} , T_{B2} , T_{B3} , and T_{B15} correspond to brightness temperatures of the AMSU-A channels 1, 2, 3, and 15, respectively, and the coefficients a , b , c , and d are obtained from the ATOVS and AVHRR pre-processing package [44]. If $I_S > 16$, then the corresponding data from AMSU-A channels 1–8 are removed.

The difference between the observed (O) and simulated (B) brightness temperatures of AMSU-A channel 4 is taken as the second criteria. If the $|O - B|$ of AMSU-A channel 4 is >1.2 K, then the data from AMSU-A channels 1–8 are rejected as cloudy data. This criterion is also applied to locate cloudy data over land: if $|O - B|$ is >1.5 K, then the data from AMSU-A channel 7 are defined as cloudy data and the data from AMSU-A channels 1–6 are not assimilated, irrespective of whether they are in a clear sky or cloudy region.

Figure 3 shows the spatial distribution of AMSU-A data from the MetOp-A satellite assimilated by the GRAPES system in southeast Asia after cloud detection using the one-stream method and the method currently used in GRAPES during the time period 0900–1500 h UTC on 8 August 2019. The green circles are the data retained by both methods, the blue circles represent the data retained by the new method only and the red circles are the data retained by the GRAPES method only. The LWP and IWP retrieved from observations of AMSU-A and MHS onboard the MetOp-A satellite are shown as shaded areas. The new method retains more AMSU-A observations, especially over the Indian Ocean, where the scattering index identifies all the area as cloudy. In the ocean to the east of China, the new detection method retains AMSU-A data over the clear sky area between the two typhoons. Apart from some data rejected by the new method in the south of Indonesia, the two methods show good consistency.

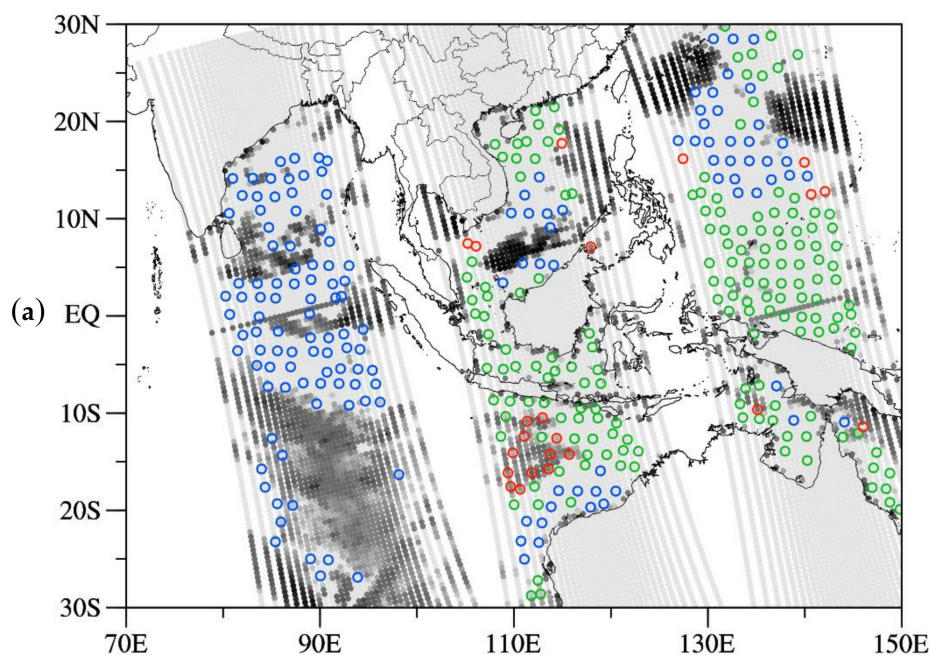


Figure 3. Cont.

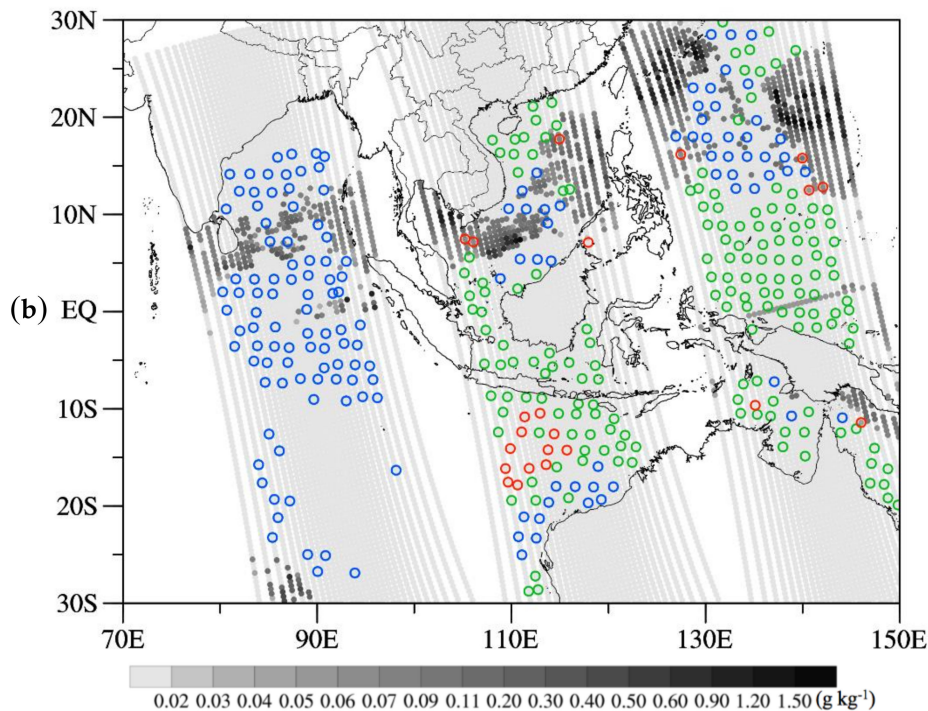


Figure 3. Spatial distribution of the data from the AMSU-A onboard the MetOp-A satellite assimilated by the GRAPES system at 0900 UTC 8 August 2019. The green circles are the data retained by both cloud detection methods, the blue circles are the data retained only by the new method and the red circles are the data retained only by the current GRAPES method. The shaded areas represent the (a) LWP and (b) IWP retrieved from the observations of the AMSU-A and MHS onboard the MetOp-A satellite during the time period 0900–1500 UTC 8 August 2019.

4. Experimental Design and Analysis of Batch Assimilation Test Results

To test the impact of the new cloud detection method on the forecast of the GRAPES system, two assimilation experiments were conducted: a control experiment (CTRL) using the GRAPES cloud detection scheme and a sensitivity experiment (ODS) using the one-stream cloud detection scheme. To be as similar as possible to the operational experiments, we conducted the experiments using the Sugon supercomputer at the China Meteorological Administration. Both sets of experiments contained both conventional data and satellite data for operational assimilation, such as AMSU-A, AIRS, ATMS, MWTS, and MWHS. All the settings followed the operational run scenario, except for the AMSU-A data. Only the AMSU-A data from the NOAA-19 and MetOp-A/B satellites were assimilated and the procedures for bias correction and quality control were consistent for both experiments, although the cloud detection scheme was different. The experiments started at 0300 UTC on 7 August and ended at 2100 UTC 10 August 2019. The six-hour forecast from the previous forecast was used as the background field for the next forecast and the 168-h forecasts were made after each assimilation.

Two typhoons appeared in the ocean to the east of China on 8 August 2019. The typhoon closest to China was Lekima, which was generated in the ocean to the northeast of the Philippines and was officially upgraded to a typhoon at 1300 UTC 7 August 2019 and then further upgraded to a super typhoon by the National Meteorological Center at 0700 UTC 8 August. The typhoon moved along the east coast of China and made landfall in Zhejiang province at 2100 UTC 10 August 2019. The maximum wind speed near the center of the typhoon reached 52 m/s, which meant that it was the strongest typhoon to make landfall in China until 2019. Typhoon Rosa was generated from a tropical disturbance to the northwest of Guam and was officially upgraded to a typhoon on 8 August 2019. Rosa moved northwest before turning into the Sea of Japan to the south of Japan, made landfall in Japan on the morning of August 15 and died out after 16 August.

The experiment starting from 0900 UTC 8 August 2019 was selected to analyze the impact of the two cloud detection methods on the forecast of the two typhoons. Figure 4 shows the air temperature and wind vector analyses for the ODS experiment at 500 hPa (Figure 4a) and 700 hPa (Figure 4b) at 0900 UTC 8 August 2019 and the spatial distribution of the difference in the air temperature analyses between the two experiments in southeast Asia. Figure 3 shows that the new method retains more observations over the ocean to the east of China and in the Indian Ocean and there are significant differences in the air temperature analysis in these two areas. The 700-hPa air temperature is lower in the ODS experiment than in the CTRL experiment in the ocean to the east of China, but the difference was reversed at 500 hPa, where the air temperature of the ODS experiment was higher than that of the CTRL experiment.

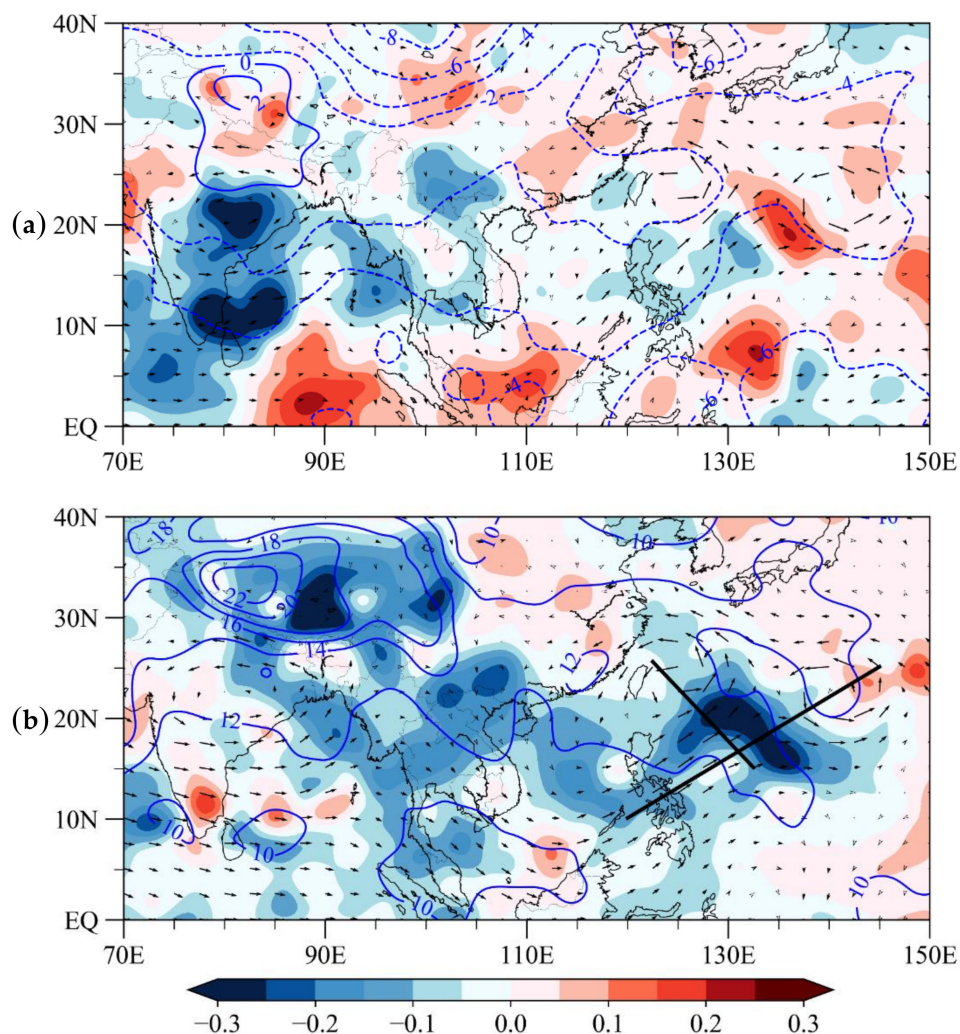


Figure 4. Spatial distribution of the air temperature (contours; units: °C) and winds (vectors; units: m/s) at (a) 500 and (b) 700 hPa for the ODS experiment at 0900 UTC 8 August 2019. The shading represents the difference in the air temperature between the two experiments (ODS–CTRL; units: °C).

Figure 5 presents cross-sections of the differences in the air temperature and geopotential height analyses between the two experiments (ODS–CTRL) at 0900 h UTC on 8 August 2019 to further clarify the impact of the increased assimilation of observations on the air temperature analysis. The location of the cross-sections is shown by the black line in Figure 4b, with the southeast–northwest line corresponding to the (a) and the southwest–northeast line corresponding to the (b). The temperature differences show a vertical distribution between the positive and negative phases; both cross-sections have negative temperature differences below 500 hPa, with a large value center located near 700 hPa.

This means that the negative differences in the air temperature analysis are probably caused by the assimilation of the extra observations from AMSU-A channel 5, the peak weighting function of which is around 700 hPa. The differences in geopotential height of these two cross-sections show a good consistency. For the atmosphere below 700 hPa, the geopotential height in the ODS experiment is increased in the areas corresponding to the negative temperature differences at this height, but for the upper atmosphere above 700 hPa, the geopotential height is decreased obviously, the negative differences are up to -4 gpm, with the center mainly located at 200 hPa.

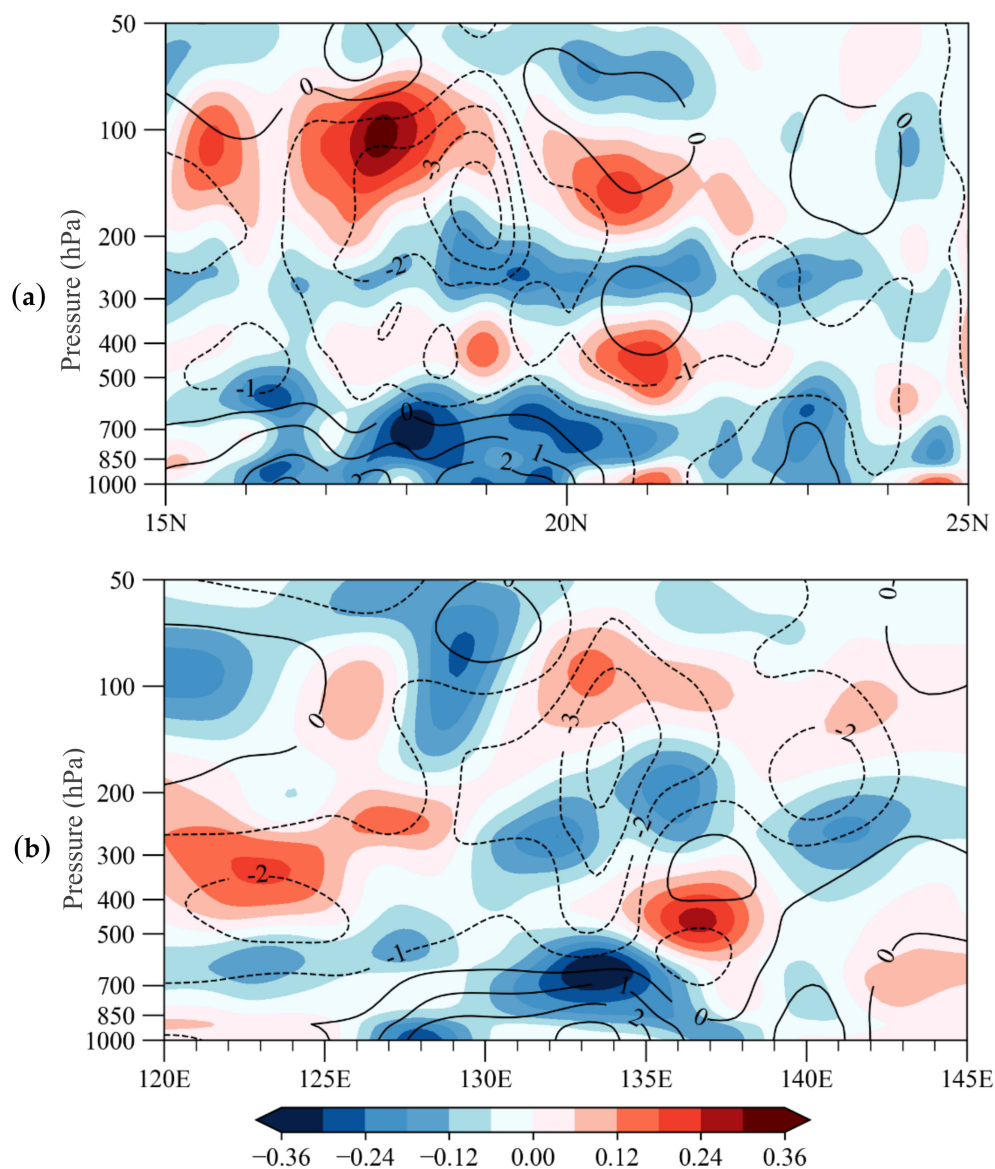


Figure 5. Cross-sections of differences in the analyses of the air temperature (shaded; units: $^{\circ}\text{C}$) and the geopotential height (contours; units: gpm) between the two experiments (ODS–CTRL) at 0900 UTC 8 August, 2019. The location of the cross-sections is shown by the black line in Figure 4b, with the southeast–northwest line corresponding to the (a) and the southwest–northeast line corresponding to the (b).

However, it should be pointed out that because the cloud top temperature is generally lower than the low-level atmospheric temperature, if the data of channel 5 in the cloud area is assimilated by accident, it may also lead to negative temperature increment in the low-level atmosphere. However, LWP and IWP retrieval methods have been applied in operational, and the above comparison results

with MODIS products also prove the correctness of the new method. In addition, the long-term performance evaluation results of the GRAPES model also show that the lower atmospheric temperature of GRAPES has a positive systematic bias [45], so the negative temperature analysis increment in the low-level atmosphere here also conforms to the model error characteristics. Therefore, we have reason to believe that the negative temperature increment is caused by correct assimilation of clear sky data.

Figure 6 shows the spatial distribution of the sea level pressure (SLP) for Lekima and Rosa at the 0900 h UTC on 8 August 2019 and the difference in SLP between the ODS and CTRL experiments (ODS–CTRL). The initial module of the typhoon is included in GRAPES, so the forecast typhoon centers are consistent with the observations in the initial stage, the best track data of typhoons come from the Typhoon Network of the National Meteorological Center (<http://typhoon.nmc.cn/web.html>). The new cloud detection method provides a positive adjustment with a maximum of 0.4 hPa to the SLP to the south of the two typhoon centers, which is consistent with the results in Figure 5.

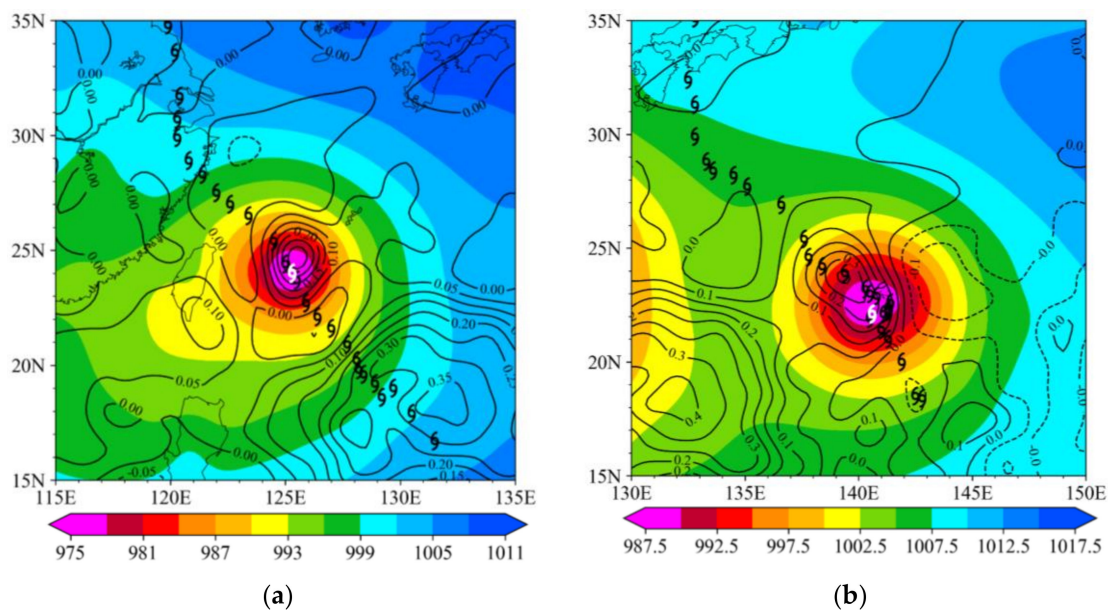


Figure 6. Spatial distribution of the SLP (shaded, units: hPa) for the CTRL experiment at 0900 UTC 8 August 2019 and the SLP difference between ODS and CTRL (contours at 0.05 hPa interval, ODS–CTRL). The observed central positions of typhoons (a) Lekima and (b) Rosa are indicated by typhoon markers; the white typhoon markers represent the central positions at the current time.

Figure 7a,b show the spatial distribution of differences in the SLP forecast between the ODS and CTRL experiments at the three- and 57-h forecasts, respectively. The difference is not significant for the three-hour forecast. However, the low center of the SLP (solid contours) in the ODS experiment is clearly further north than that in the CTRL experiment (dashed contours) for the 57-h forecast and is also closer to the observed center of the typhoon. This indicates that the lower air temperature and higher pressure to the southeast of the typhoon led to an increase in the speed of movement of the typhoon in the ODS forecast.

Rosa had been rotating near the place where it was generated in the early stages of formation, so the speed of movement was significantly slower than that of Lekima, which increased the difficulty of the forecast. Rosa moved northward on 12 August, 2019 and approached southern Japan. Figure 7c,d show the SLP forecast of the ODS and CTRL experiments at 105 and 123 h. Both forecasts show premature turning and the forecast typhoon centers are further to the east than the observed centers, although the low center of the SLP in the ODS experiment is closer to the observations. The improved effect of the new method becomes clearer with an increase in the forecast time.

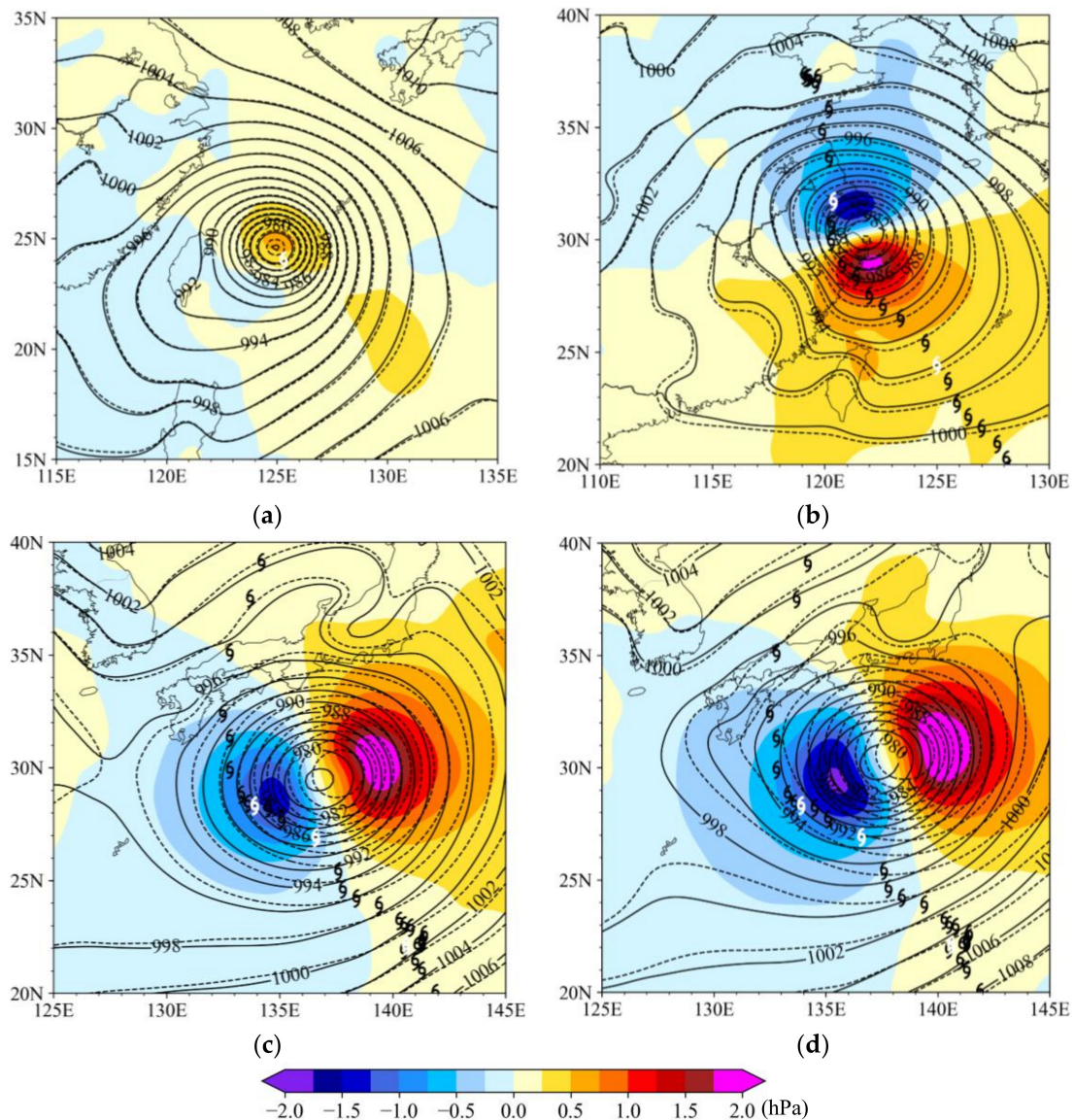


Figure 7. Spatial distribution of the forecasted SLP of ODS (solid contours at 2-hPa interval) and CTRL (dashed contours at 2-hPa interval) and their differences (ODS-CTRL, shaded) at (a) 1200 UTC 8 August 2019 (3-h forecast), (b) 1800 UTC 10 August 2019 (57-h forecast), (c) 1800 UTC 12 August 2019 (105-h forecast) and (d) 1200 UTC 13 August 2019 (123-h forecast). The locations of the observed centers of (a,b) Lekima and (c,d) Rosa are indicated by typhoon markers; the white typhoon markers represent the central positions at that particular time.

Forecasts of the geopotential height at 500 hPa were further evaluated by comparison with the final analysis (FNL) data [46]. Figure 8 shows the mean bias (solid curves) and standard deviation (dashed curves) of the difference between the forecasts and the FNL data (FNL-CTRL, FNL-ODS) with the forecast time for the geopotential height at 500 hPa and the air temperature at 300 hPa. The blue curves represent the difference between the ODS and the FNL data (FNL-ODS), whereas the black curves represent the differences between the CTRL forecast and the FNL data (FNL-CRL). Figure 8a shows that with an increase in the forecast time, the mean bias remained slightly positive (about 2 gpm) for the first 110 h, but then quickly shifted to a negative bias as high as -8 gpm, while the standard deviation gradually increased. The mean bias and the standard deviation of the two experiments were similar in the first 110 h, after which the bias and standard deviation of the ODS experiment were stable, but smaller, than in the CTRL experiment.

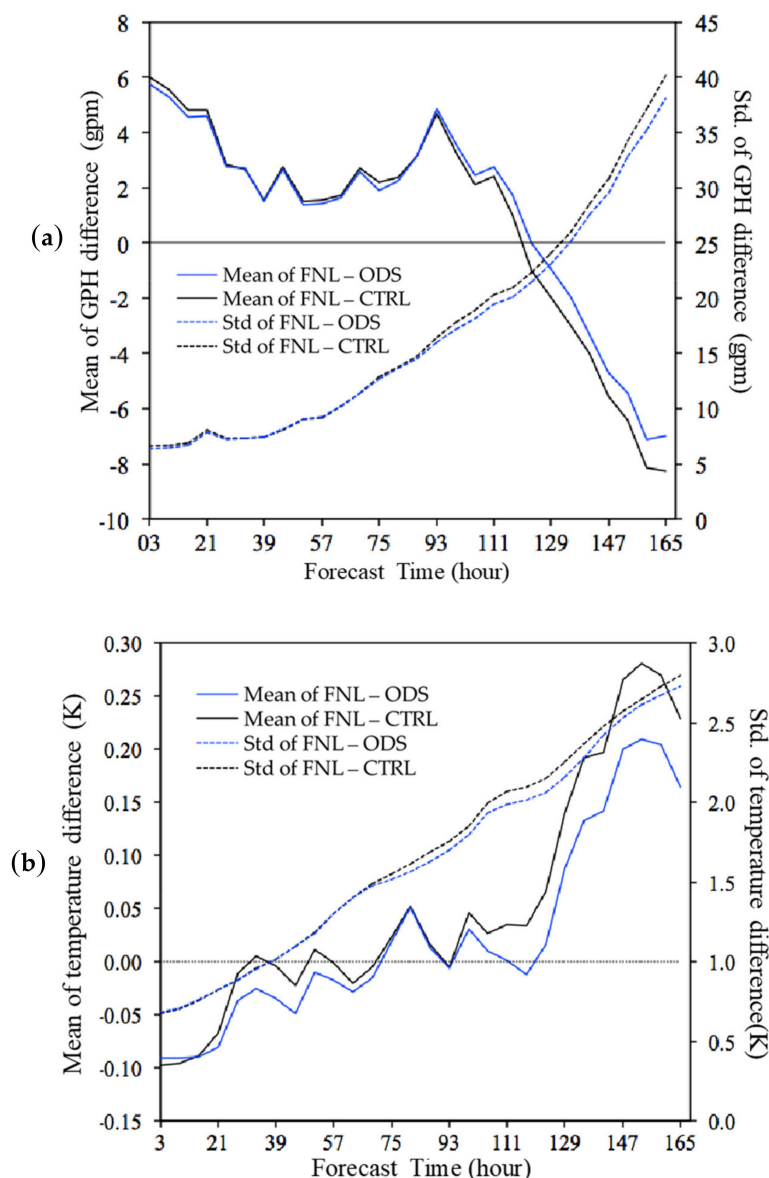


Figure 8. Mean (solid lines) and standard deviation (dashed lines) of the differences of (a) geopotential height at 500 hPa and (b) atmospheric temperature at 300 hPa between the ODS/CTRL forecasts and the FNL forecasts (FNL-ODS, blue lines; FNL-CTRL, black lines) varying with the forecast time in the region (20–60°N, 0–360°E).

Similar to the results for the geopotential height at 500 hPa, the turning point for the bias of the air temperature at 300 hPa also occurred at about 110 h, before which the mean bias fluctuated around the zero value for both experiments. The bias rapidly changed to a positive value after 110 h, which could be as high as 0.25 K. The ODS experiment gave better results than the CTRL experiment after 110 h for both the mean bias and the standard deviation. This indicates that our new method can reduce the rapid growth of the error in the later period of forecasts.

Figure 9 shows the biases (Figure 9a) and standard deviations (Figure 9b) for the vertical differences in air temperature between the FNL and forecast (FNL-ODS, solid lines; FNL-CTRL, dashed lines) data at three (black curves), 81 (red curves) and 165 (blue curves) forecast hours in the region (20–60°N, 0–360°E). The difference between the two experiments becomes increasingly evident with the increase in forecast time. Figure 9b shows that the improvement effect first appears at 200–700 hPa and then expands to all levels of the model; this corresponds well with the results of the previous incremental analysis in Figures 4 and 5.

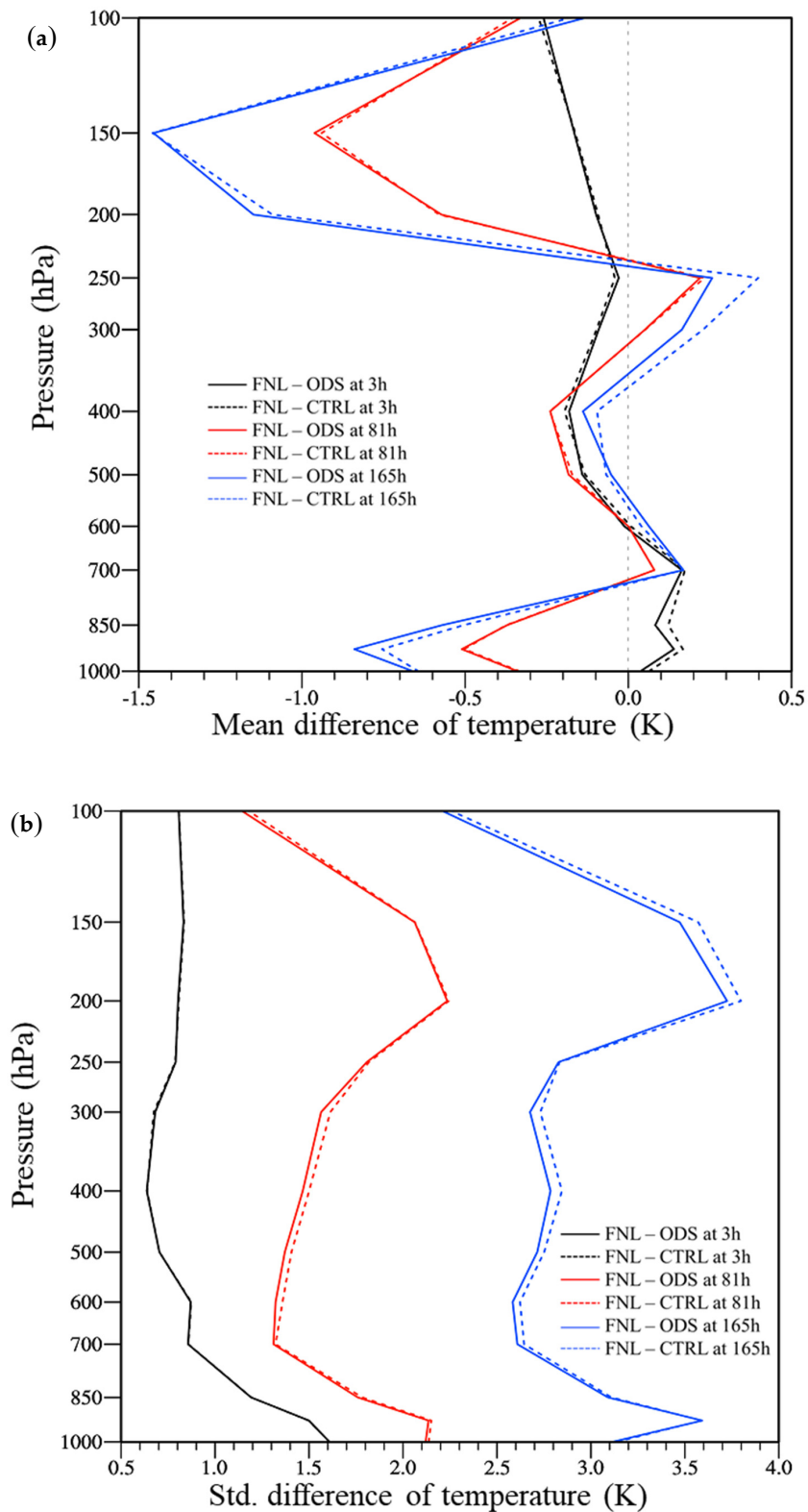


Figure 9. (a) Mean biases and (b) standard deviations of the vertical differences of temperature between the FNL and forecast data (FNL-ODS, solid lines; FNL-CTRL, dashed) at 3 (black lines), 81 (red lines) and 165 (blue lines) different forecast times in the region (20–60°N, 0–360°E).

An overall evaluation of the level of forecasts for large-scale weather systems is given by the anomaly correlation coefficient (ACC) of the 500 hPa height forecasts. Figure 10 gives the mean value

of the ACC of the 500 hPa geopotential height between the FNL and three-hour forecasts of the ODS (blue) and CTRL (red) experiments from 0900 UTC 8 August 2019 to 0900 UTC 9 August 2019. The blue histograms represent the 95% confidence levels. The ACCs of the two experiments decrease with the increase in forecast time, but the ACCs of the ODS experiment are higher than those of the CTRL experiment from 12 h. The improvement effect became clearer with the increase in forecast time and the differences in the ACC were significant from 120 h.

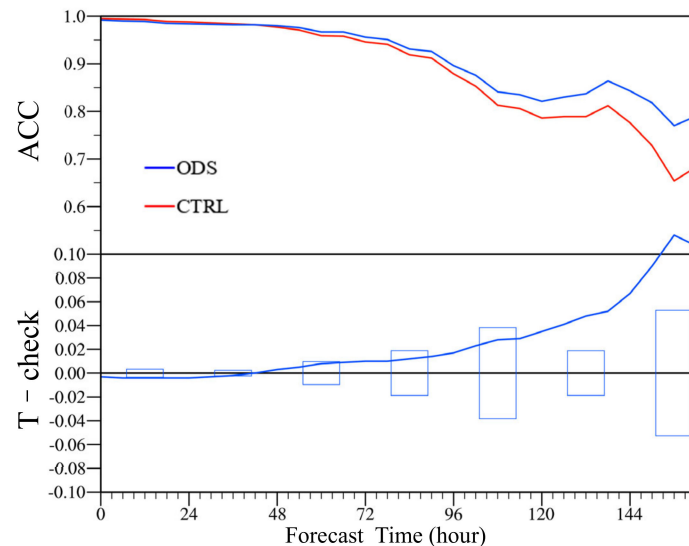


Figure 10. The ACC of the geopotential height at 500 hPa in the northern hemisphere between the FNL data and the forecasts of the two experiments (blue curve is for ODS experiment, red curve is for the CTRL) from 0900 UTC 8 August to 0900 UTC 9 August 2019. The blue curve is the ACC difference between ODS and CTRL (ODS–CTRL), the blue histograms represent the 95% confidence levels.

The comparison results of the ACC were similar for the 6-h interval rolling experiments from 7 to 10 August 2019 (Figure 11), but the improvement was relatively weak. The ACC was improved by the new cloud detection system from 48 h and the improvement effect became increasingly clear with the increase in forecast time, and the differences pass the significant test after 144 h, which shows that the new method has a significant positive impact on the forecast of the GRAPES.

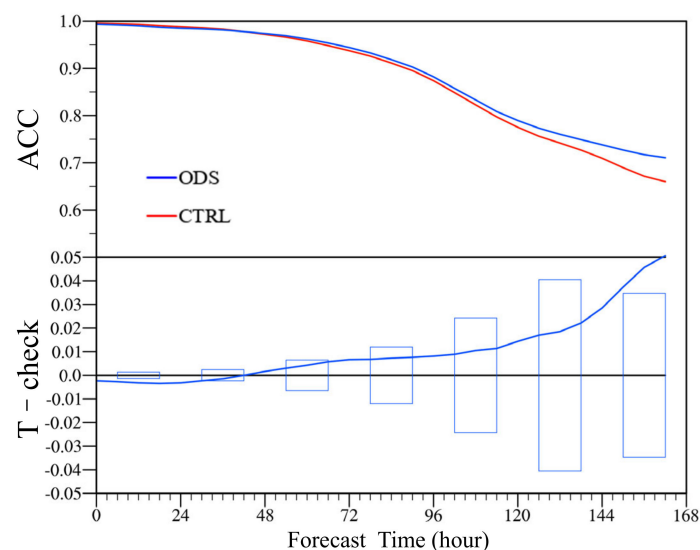


Figure 11. Same as Figure 10 except for the ACC between the FNL data and the rolling forecasts of the two experiments from 0300 UTC 7 August 2019 to 2100 UTC 10 August 2019 at 6-h intervals.

5. Discussion and Conclusions

The AMSU-A and MHS have both been onboard the polar-orbiting NOAA-18 satellite since it was launched, but the data from the two instruments have always been assimilated separately. We merged the data from the two instruments by matching nine MHS FOVs to one AMSU-A FOV and combined the LWP and IWP retrieved from the two instruments to provide a more accurate cloud detection method for the AMSU-A data.

The new cloud detection method was implemented in GRAPES and four-day rolling experiments were conducted to evaluate its impact. The results show that the new cloud detection method can accurately identify cloud radiance and retain more observations than the method currently used in the GRAPES system. The assimilation of the extra AMSU-A data improved the track forecast of typhoon Lekima by adjusting the air temperature and potential height fields at the center and periphery of the typhoon. The error in premature turning was reduced for the forecast of the track of typhoon Rosa, which moved the forecast track closer to the observed track.

The effect of the new method on the forecast of two large-scale weather systems was also examined by comparing the forecasts with the FNL analysis data. The results show that both the mean bias and the standard deviation of the air temperature and geopotential height forecasts are reduced in the new method and the improvement becomes clearer with an increase in the forecast time. The ACCs of the 500 hPa height forecasts are also increased in the new method for both the case results and rolling forecasts. All our results show that the new method can improve the GRAPES forecast of large-scale weather systems.

This study shows the positive impact of the one-stream cloud detection method on GRAPES forecasts by improving the quality control of the AMSU-A data. The potential value of this method will be further explored by applying it to the microwave temperature sounder and MHS onboard polar-orbiting satellites in the Chinese FY-3 series.

Author Contributions: Conceptualization, Z.Q.; data curation, Z.W.; formal analysis, Z.Q.; funding acquisition, Z.Q. and J.L.; investigation, Z.Q.; methodology, Z.Q.; project administration, Z.Q. and J.L.; resources, Z.W.; software, Z.Q. and Z.W.; validation, Z.Q.; visualization, Z.Q. and Z.W.; writing—original draft, Z.Q. and Z.W.; writing—review & editing, Z.Q., Z.W., and J.L. All authors have read and agreed to the published version of the manuscript.

Funding: This research was jointly funded by the National Key R&D Program of China (Grant 2018YFC1507302) and the Nanjing Joint Center of Atmospheric Research Program (Project NJCAR2018ZD01).

Acknowledgments: The authors would like to acknowledge the Numerical Weather Prediction Center of CMA for providing the latest version of GRAPES and supercomputer computing resources.

Conflicts of Interest: The authors declare no conflict of interest.

References

1. Eyre, J.; Kelly, G.A.; McNally, A.; Andersson, E. Assimilation of TOVS radiance information through one-dimensional variational analysis. In *ECMWF Technical Memoranda*; ECMWF: Shinfield Park, UK, 1992; p. 31.
2. Xue, J.S. Scientific issues and perspective of assimilation of meteorological satellite data. *Acta Meteor. Sin.* **2009**, *67*, 903–911. (In Chinese)
3. Kidwell, K. *NOAA Polar Orbiter Data User's Guide*. 1998; NCDC/SDSD, National Climatic Data Center: Washington, DC, USA, 1991.
4. NOAA. *User's Guide (Satellite and Data Description of NOAA's Polar Orbiting Satellites from NOAA-15 and Later)*; NOAA, NCDC: Asheville, NC, USA, 2009.
5. Weng, F.; Zou, X.; Wang, X.; Yang, S.; Goldberg, M.D. Introduction to Suomi national polar-orbiting partnership advanced technology microwave sounder for numerical weather prediction and tropical cyclone applications. *J. Geophys. Res. Atmos.* **2012**, *117*, 1–14. [[CrossRef](#)]
6. Li, J.; Qin, Z.; Liu, G. A new generation of Chinese FY-3C microwave sounding measurements and the initial assessments of its observations. *Int. J. Remote. Sens.* **2016**, *37*, 4035–4058. [[CrossRef](#)]

7. Okamoto, K.; Kazumori, M.; Owada, H. The Assimilation of ATOVS Radiances in the JMA Global Analysis System. *J. Meteor. Soc. Jpn.* **2005**, *83*, 201–217. [[CrossRef](#)]
8. English, S.J.; Renshaw, R.J.; Dibben, P.C.; Smith, A.J.; Rayer, P.J.; Poulsen, C.; Saunders, F.W.; Eyre, J.R. A comparison of the impact of TOVS arid ATOVS satellite sounding data on the accuracy of numerical weather forecasts. *Q. J. R. Meteorol. Soc.* **2000**, *126*, 2911–2931. [[CrossRef](#)]
9. Zapotocny, T.H.; Jung, J.A.; Le Marshall, J.F.; Treadon, R.E. A Two-Season Impact Study of Four Satellite Data Types and Rawinsonde Data in the NCEP Global Data Assimilation System. *Weather Forecast.* **2008**, *23*, 80–100. [[CrossRef](#)]
10. Andersson, E.; Pailleux, J.; Thépaut, J.-N.; Eyre, J.R.; McNally, A.P.; Kelly, G.A.; Courtier, P. Use of cloud-cleared radiances in three/four-dimensional variational data assimilation. *Q. J. R. Meteorol. Soc.* **1994**, *120*, 627–653. [[CrossRef](#)]
11. Derber, J.C.; Wu, W.-S. The Use of TOVS Cloud-Cleared Radiances in the NCEP SSI Analysis System. *Mon. Weather Rev.* **1998**, *126*, 2287–2299. [[CrossRef](#)]
12. McNally, A.P.; Watts, P.D.; Smith, J.A.; Engelen, R.; Kelly, G.A.; Thépaut, J.N.; Matricardi, M. The assimilation of AIRS radiance data at ECMWF. *Q. J. R. Meteorol. Soc.* **2006**, *132*, 935–957. [[CrossRef](#)]
13. Karbou, F.; Gérard, É.; Rabier, F. Microwave land emissivity and skin temperature for AMSU-A and -B assimilation over land. *Q. J. R. Meteorol. Soc.* **2006**, *132*, 2333–2355. [[CrossRef](#)]
14. Shen, F.; Min, J. Assimilating AMSU-a radiance data with the WRF hybrid En3DVAR system for track predictions of Typhoon Megi (2010). *Adv. Atmos. Sci.* **2015**, *32*, 1231–1243. [[CrossRef](#)]
15. Qin, Z.; Zou, X. Development and initial assessment of a new land index for microwave humidity sounder cloud detection. *J. Meteorol. Res.* **2016**, *30*, 12–37. [[CrossRef](#)]
16. Liu, Y.; Xue, J.S.; Zhang, L. Verification and Diagnostics for Data Assimilation System of Global GRAPES. *J. Appl. Meteor. Sci.* **2016**, *27*, 1–15. (In Chinese)
17. Zhang, H.; Xue, J.S.; Zhang, S.Y. Idea Experiments of GRAPES Three-Dimensional Vibrational Data Assimilation System. *Acta Meteor. Sinica.* **2004**, *1*, 31–41. (In Chinese)
18. Bauer, P.; Auligné, T.; Bell, W.; Geer, A.; Guidard, V.; Heilliette, S.; Kazumori, M.; Kim, M.-J.; Liu, E.H.-C.; McNally, A.P.; et al. Satellite cloud and precipitation assimilation at operational NWP centres. *Q. J. R. Meteorol. Soc.* **2011**, *137*, 1934–1951. [[CrossRef](#)]
19. McNally, A.P. The direct assimilation of cloud-affected satellite infrared radiances in the ECMWF 4D-Var. *Q. J. R. Meteorol. Soc.* **2009**, *135*, 1214–1229. [[CrossRef](#)]
20. Bormann, N.; Bauer, P. Estimates of spatial and interchannel observation-error characteristics for current sounder radiances for numerical weather prediction. I: Methods and application to ATOVS data. *Q. J. R. Meteorol. Soc.* **2010**, *136*, 1036–1050. [[CrossRef](#)]
21. Geer, A.J.; Bauer, P. Observation errors in all-sky data assimilation. *Q. J. R. Meteorol. Soc.* **2011**, *137*, 2024–2037. [[CrossRef](#)]
22. Bouchard, A.; Rabier, F.; Guidard, V.; Karbou, F. Enhancements of Satellite Data Assimilation over Antarctica. *Mon. Weather Rev.* **2010**, *138*, 2149–2173. [[CrossRef](#)]
23. Zou, X.; Qin, Z.; Zheng, Y. Improved Tropical Storm Forecasts with GOES-13/15 Imager Radiance Assimilation and Asymmetric Vortex Initialization in HWRF. *Mon. Weather Rev.* **2015**, *143*, 2485–2505. [[CrossRef](#)]
24. Karbou, F.; Gérard, E.; Rabier, F. Global 4DVAR Assimilation and Forecast Experiments Using AMSU Observations over Land. Part I: Impacts of Various Land Surface Emissivity Parameterizations. *Weather Forecast.* **2010**, *25*, 5–19. [[CrossRef](#)]
25. Karbou, F.; Rabier, F.; Lafore, J.-P.; Redelsperger, J.-L.; Bock, O. Global 4DVAR Assimilation and Forecast Experiments Using AMSU Observations over Land. Part II: Impacts of Assimilating Surface-Sensitive Channels on the African Monsoon during AMMA. *Weather Forecast.* **2010**, *25*, 20–36. [[CrossRef](#)]
26. Auligné, T.; McNally, A.P.; Dee, D.P. Adaptive bias correction for satellite data in a numerical weather prediction system. *Q. J. R. Meteorol. Soc.* **2007**, *133*, 631–642. [[CrossRef](#)]
27. Liu, Z.; Schwartz, C.S.; Snyder, C.; Ha, S.-Y. Impact of Assimilating AMSU-A Radiances on Forecasts of 2008 Atlantic Tropical Cyclones Initialized with a Limited-Area Ensemble Kalman Filter. *Mon. Weather Rev.* **2012**, *140*, 4017–4034. [[CrossRef](#)]
28. Bennartz, R.; Thoss, A.; Dybbroe, A.; Michelson, D.B. Precipitation analysis using the Advanced Microwave Sounding Unit in support of nowcasting applications. *Met. Apps.* **2002**, *9*, 177–189. [[CrossRef](#)]

29. Zou, X.; Weng, F.; Zhang, B.; Lin, L.; Qin, Z.; Tallapragada, V. Impacts of assimilation of ATMS data in HWRF on track and intensity forecasts of 2012 four landfall hurricanes. *J. Geophys. Res. Atmos.* **2013**, *118*, 11558–11576. [[CrossRef](#)]
30. Zou, X.; Qin, Z.; Weng, F. Impacts from assimilation of one data stream of AMSU-A and MHS radiances on quantitative precipitation forecasts. *Q. J. R. Meteorol. Soc.* **2017**, *143*, 731–743. [[CrossRef](#)]
31. Huang, L.P.; Wu, X.J.; Jin, Z.Y. Schemes and Application of GRAPES Model Standard Initialization. *J. Appl. Meteor. Sci.* **2005**, *16*, 374–384. (In Chinese)
32. Chen, D.H.; Shen, X.S. Recent Progress on GRAPES Research and Application. *J. Appl. Meteor. Sci.* **2006**, *17*, 773–777. (In Chinese)
33. Zhang, R.H.; Shen, X.S. Development of Chinese New Generation Operational Numerical Forecast System: GRAPES. *Chin. Sci. Bull.* **2008**, *53*, 2393–2395. (In Chinese)
34. Xue, J.S.; Zhang, S.Y.; Zhu, G.F. GRAPES Next Generation Global/Regional Variable Differentiation and Assimilation System Study. *Chin. Sci. Bull.* **2008**, *53*, 2408–2417. (In Chinese)
35. Zhang, S.Y.; Xue, J.S.; Zhu, G.F. GRAPES Global 3D Var System-Basic Scheme Design and Single Observation Test. *Chin. J. Atmos. Sci.* **2005**, *29*, 30–42. (In Chinese)
36. Zhang, H.; Xue, J.; Zhu, G.; Zhuang, S.; Wu, X.; Zhang, F. Application of direct assimilation of ATOVS microwave radiances to typhoon track prediction. *Adv. Atmos. Sci.* **2004**, *21*, 283–290. [[CrossRef](#)]
37. Li, J.; Liu, G. Direct assimilation of Chinese FY-3C Microwave Temperature Sounder-2 radiances in the global GRAPES system. *Atmos. Meas. Tech.* **2016**, *9*, 3095–3113. [[CrossRef](#)]
38. Zhang, L.; Liu, Y.Z. The Preconditioning of Minimization Algorithm in GRAPES Global Four-dimensional Variation Data Assimilation System. *J. Appl. Meteor. Sci.* **2017**, *28*, 168–176. (In Chinese)
39. Liu, Y.; Xue, J.S. The New Initialization Scheme of the GRAPES. *Acta Meteor. Sin.* **2019**, *77*, 165–179. (In Chinese)
40. Grody, N.; Zhao, J.; Ferraro, R.; Weng, F.; Boers, R. Determination of precipitable water and cloud liquid water over oceans from the NOAA 15 advanced microwave sounding unit. *J. Geophys. Res.* **2001**, *106*, 2943–2953. [[CrossRef](#)]
41. Weng, F.; Zhao, L.; Ferraro, R.R.; Poe, G.; Li, X.; Grody, N.C. Advanced microwave sounding unit cloud and precipitation algorithms. *Radio Sci.* **2003**, *38*. [[CrossRef](#)]
42. Rossow, W.B.; Walker, A.W.; Beuschel, D.E.; Roiter, M.D. *International Satellite Cloud Climatology Project (ISCCP) Documentation of New Cloud Datasets*; WMO/TD 737; World Meteorological Organization: Geneva, Switzerland, 1996; p. 115.
43. Platnick, S.; Ackerman, S.; King, M. *MODIS Atmosphere L2 Cloud Product (06_L2)*; NASA MODIS Adaptive Processing System, Goddard Space Flight Center: Greenbelt, MD, USA, 2015; Volume 10, pp. 1–53.
44. Labrot, T.; Lavanant, L.; Whyte, K.; Atkinson, N.; Brunel, P. AAPP Documentation. Scientific Description, NWP SAF Satellite Application Facility for Numerical Weather Prediction; Document NWPSAF-MF-UD-001, Version 7.0; October 2011. Available online: https://nwpsaf.eu/site/download/documentation/aapp/NWPSAF-MF-UD-001_Science.pdf (accessed on 20 November 2019).
45. Meng, Z.; Haipeng, Y.; Jianping, H.; Xueshun, S.; Yong, S.; Haile, X.; Baocheng, D. Assessment on Unsystematic Errors of GRAPES_GFS 2.0. *J. Appl. Meteorol. Sci.* **2018**, *29*, 571–583.
46. National Centers for Environmental Prediction. National Centers for Environmental Prediction. National Centers for Environmental Prediction/National Weather Service/NOAA/US Department of Commerce. 2000, updated daily. In *NCEP FNL Operational Model Global Tropospheric Analyses, Continuing from July*; National Centers for Environmental Prediction: Silver Spring, MD, USA, 1999.

Publisher’s Note: MDPI stays neutral with regard to jurisdictional claims in published maps and institutional affiliations.



© 2020 by the authors. Licensee MDPI, Basel, Switzerland. This article is an open access article distributed under the terms and conditions of the Creative Commons Attribution (CC BY) license (<http://creativecommons.org/licenses/by/4.0/>).